



OPEN Deep magma sources beneath Central Kamchatka inferred from teleseismic tomography

Ivan Koulakov^{1,2}✉, Olga Bergal-Kuvikas^{3,4}, Maria Voronova² & Andrey Jakovlev⁵

Central Kamchatka is a typical Andean-type subduction complex including a linear volcanic arc, back-arc volcanic complexes and zones of tectonic shortening and extension. With the use of teleseismic tomography, we investigate the role of mantle processes in the observed volcanic and tectonic activity in this region. We use the seismic data of permanent stations and a temporary network deployed in central Kamchatka in 2019–2020. Arrival times of the P waves from events at distances from 15 to 110 degrees are used as input for tomographic inversion to derive a 3D model of the P-wave velocity anomalies down to the depth of 150 km. In the resulting model, beneath the central part of the study area, we observe a prominent low-velocity anomaly in the mantle overlain by a high-velocity crustal block. A chain of the Avacha Group volcanoes is located above the northeastern border of this anomaly, and Mutnovsky, Gorely and Viluchinsky volcanoes are associated with its southwestern border. We propose that the hot mantle material, which arrived from the slab window, surrounds the bottom of the rigid crustal block and ascend along its borders causing the formation of large stratovolcanoes.

Abbreviations

MPZ	Malko-Petropavlovsk fault zone
KBGS	Kamchatka Branch of Geophysical Survey of Russian Academy of Sciences
LSQR	Least square method with QR factorization
LET	Local earthquake tomography
ANT	Ambient noise tomography

Kamchatka is the large Peninsula in the Far East of Russia located in the north-western corner of the Pacific Ocean (Fig. 1B). Most of Kamchatka's territory remains inhabited and has a very poor road infrastructure. The eastern coast of Central Kamchatka is the only region with a relatively dense population living in the major cities of Kamchatka, namely Petropavlovsk-Kamchatsky, Elizovo and Vilyuchinsk. These cities and their surrounding agglomerations accommodate approximately 250,000 inhabitants, representing around 80% of Kamchatka's population. In this study, we consider a large part of Central Kamchatka, which includes these populated areas to the east and generally non-populated areas to the west (Fig. 1A).

The tectonic and volcanic activity in Kamchatka is mostly controlled by the ongoing subduction of the Pacific Plate along the Kuril-Kamchatka and Aleutian arcs with the rate of 7.6 cm/year¹. More than a hundred of Pleistocene and Holocene volcanoes can be identified in the Kamchatka Peninsula² (Fig. 1B), of which ~41 exhibited eruption activity in historical times³. A broad range of compositions and eruption regimes of the arc volcanoes infers that they are fed through a complex system of magma sources in the crust and mantle wedge that were initially originated on the upper boundary of the dehydrating subducted slab⁴.

Systematic, multiscale studies of deep structures below such volcanic centers are important to better understand the processes of magma formation. A relatively well studied part of Kamchatka is an area located around the main city of the region, Petropavlovsk-Kamchatsky. Because of a serious hazard of earthquakes and volcanic eruptions, this area is actively studied with the use of different geophysical methods. The long-term land gravity measurements were performed since the 1960s⁵ and were compiled in a number of density models of the crust beneath the Avacha group^{6,7}. In the same area of central-eastern Kamchatka, more than 1000 measurement points of magnetotelluric sounding were collected and used to build the electrical resistivity model of the crust⁸. The deep seismic sounding was conducted in the area of Avacha volcano in the 1980s. The processing of these

¹Skolkovo Institute of Science and Technology (Skoltech), Bolshoy Blrd. 30/1, Moscow, Russia121205. ²Trofimuk Institute of Petroleum Geology and Geophysics (IPGG) SB RAS, Novosibirsk, Russia630090. ³Institute of Volcanology and Seismology, Petropavlovsk-Kamchatsky, Russia. ⁴Vitus Bering Kamchatka State University, Petropavlovsk-Kamchatsky, Russia. ⁵Alfred Wegener Institute for Polar and Marine Research, Bremerhaven, Germany. ✉email: ivan.science@gmail.com

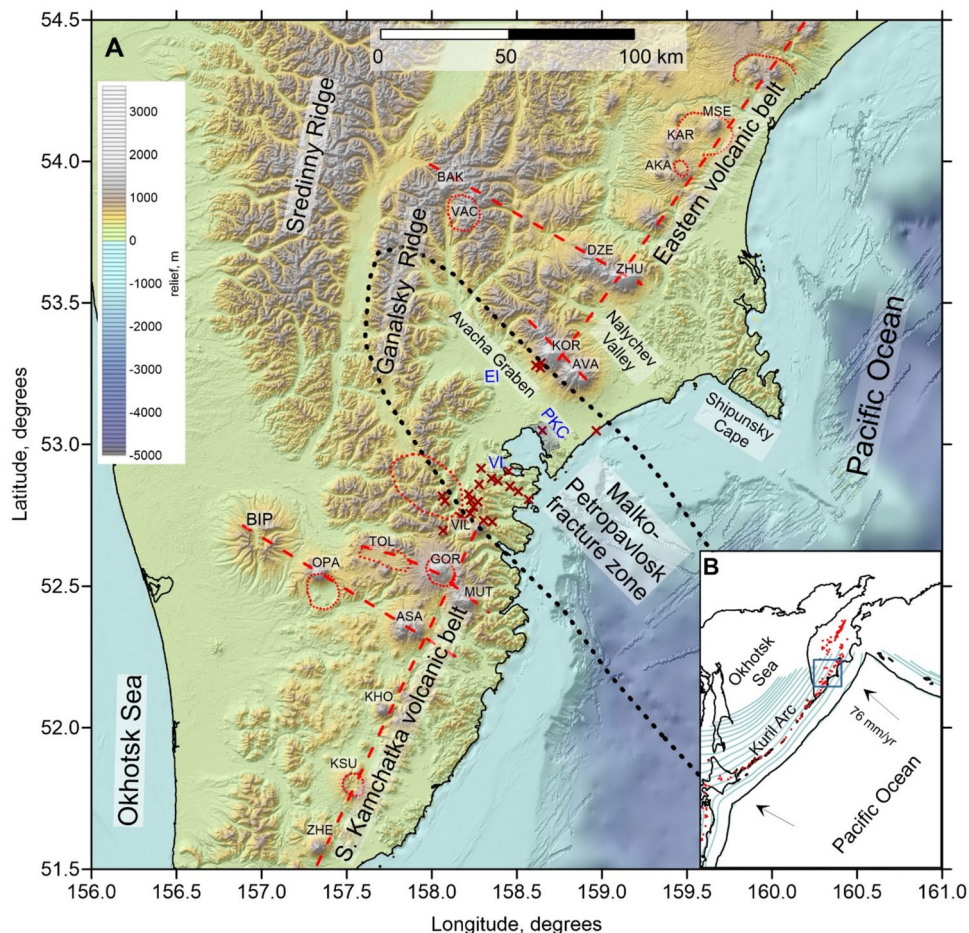


Fig. 1. Study area. **(A)** Topography and main geological structures in central Kamchatka. The red dotted line highlights major calderas. The red dashed lines indicate volcano lineaments. The red crosses indicate monogenic cones and extrusive domes within the MPZ. The main cities highlighted with blue characters: PKC—Petropavlovsk-Kamchatsky, El—Elizovo, VI—Viluchinsk. Abbreviations for volcanoes: ZHE—Zheltoivsky; KSU—Ksudach; KHO—Khodutka, ASA—Asacha; OPA—Opala; BIP—Bolshaya Ipelka; MUT—Mutnovsky; Gor—Gorely; VIL—Vil-yuchinsk, KAR—Karymshina Caldera, TOL—Tolmachev Dol; KOR—Koryaksky; AVA—Avachinsky; DZE—Dzenzur; Zhu—Zhupanovsky; VAC—Verkhneavachinskaya Caldera; BAK—Bakening; AKA—Akademii Nauk; KAR—Karymsky; MSE—Maly Semyachik. **(B)** Location of the study area (blue rectangle) in the regional map. The blue lines indicate the shape of the slab¹. The red dots depict the Holocene volcanoes². The rate of the Pacific Plate movement is indicated by arrows. The figure was generated using the software Surfer (version 13, <http://www.goldensoftware.com/products/surfer>).

data using classical methods of refraction wave analysis^{9,10} and seismic tomography¹¹ resulted in generally consistent structures with a prominent velocity contrast below Avacha Volcano.

Seismological studies of this region were initially based on the data of the permanent seismic network operated by the Kamchatka Branch of Geophysical Survey of Russian Academy of Sciences (KBGS) having a relatively good coverage in central-eastern Kamchatka¹². Large-scale tomography models based on regional and worldwide seismological catalogs clearly map the shape of the slab in the mantle^{13–15}. The smaller-scale seismic models were constructed based on the data of local permanent and temporary stations. In particular, the Avacha group of volcanoes is covered by seven stations, whose data were used to build local-earthquake tomography below Avacha and Koryaksky active volcanoes¹⁶. Later this model was considerably improved after including the data of temporary stations deployed on the Avacha group¹⁷. The data of the permanent seismic network were also used to study larger scale structures in the entire crust and upper mantle¹⁸, but the coverage of the stations did not provide sufficient data distributions; therefore, the resolution and reliability of these models were not very high. The western part of central Kamchatka could not be studied with the data of KBGS permanent network because of insufficient distributions of seismic stations there.

A significant progress in studying the deep structure beneath the entire Central Kamchatka was achieved after deploying in 2019–2020 a regional network covering an area from the eastern to western coasts between the latitudes of 52.7–54°N¹⁹. The data of these networks were previously used in an ambient-noise tomography study²⁰ to reveal the structure of the S-wave heterogeneities in the entire crust down to ~20 km. The other study¹⁹ used the arrival times of the P and S waves from the local and regional events recorded by the temporary

and permanent stations to infer the structures in the crust and in the mantle wedge. Note however, that both methods used in these studies have some limitations and uncertainties that may affect the derived velocity models. That is probably why, these two models differ considerably in an overlapping depth interval, which indicates that the information about deep structures is still not definitive and need to be corroborated with alternative approaches.

Here, we use the same dataset including the seismograms from the temporary network 2019–2020 and permanent stations in Central Kamchatka to build another model of the crustal and mantle structures based on a teleseismic tomography algorithm. This gives us a completely independent model that can be used to corroborate the previous results. Furthermore, this scheme provides more homogeneous ray distributions and does not face with a problem of the trade-off between the source and velocity parameters that exist in local earthquake tomography. It may give us a possibility to obtain more reliable results for the mantle part of the model.

Geological settings

The present geological processes of Kamchatka are mostly determined by the ongoing subduction of the Pacific Plate that occurs in the northwestern direction nearly orthogonally to the trench orientation with the rate of 7.45–7.81 cm/year¹. Kamchatka is a typical subduction complex of the Andean type, which includes a well-established deep oceanic trench, an accretion wedge, a linear volcanic arc, back-arc volcanic complexes and several zones of tectonic shortening and extension causing the origin of mountain ridges and rift valleys. At the same time, the subduction processes below Kamchatka are far from a simple 2D conveyor-type model. For example, lateral heterogeneities in the slab were presumed to cause a complex shape of the coastal line and jumps of the volcanic front²¹.

An important tectonic structure in central Kamchatka is the Malko-Petropavlovsk fault zone (MPZ) (Fig. 1A), which partly coincides with the Avacha Graben in the onshore part²². This zone of transverse dislocations represents a transition between geologically distinct structures in central and southern Kamchatka. MPZ was identified as a dislocation area that was formed during the collision of the Kronotsky block in the late Oligocene²², when the volcanic arc migrated from the coastal area to the present location of the Sredinny Range. The trench-perpendicular fractures along the MPZ can be identified on the surface from structural geological surveys²³ and at depth from the basement structures identified by different geophysical studies^{24–26}.

MPZ appears to be located at a continuation of the Avachinsky transform fault in the Pacific Plate separating the oceanic lithosphere segments of different ages^{27,28}. The area of MPZ is characterized by a series of fracture zones, which appear to be associated with hydrothermal magmatic systems²⁹. To the south of this zone, the slab-related seismicity is observed down to 600 km, whereas in the northern part, the seismicity is shallower^{21,30}. The crustal seismicity within MPZ is significantly less active than in the other coastal areas to the south and to the north³¹. The area of MPZ is characterized by relatively high mean heat flow (~80 mWt/m²) compared to the surrounding regions (40–60 mWt/m²)³². It also includes some local zones of very high geothermal activity, such as Paratunka and Koryaksko-Ketkinsky geothermal fields.

The main volcanic arc in central and southern Kamchatka (indicated by the trench-parallel red dashed lines in Fig. 1A) is composed of two nearly linear segments of Southern Kamchatka and Eastern volcanic belts. Within each of these belts, the distinct large Holocene stratovolcanoes or volcano groups are separated with regular intervals of 25–30 km: Zheltovsky—Ksudach—Khodutka—Asacha—Gorely—Vilyuchinsky in South-Kamchatka volcanic front and Avacha—Zhupanovsky—Karymsky—Maly Semyachik in the Eastern volcanic front. At the same time, some groups of volcanoes form linear chains in the direction of the subducting plate displacement, such as four lineaments indicated by trench-perpendicular red dashed lines in Fig. 1A: (1) Asacha-Opala-Bolshaya Ipeka, (2) Mutnovsky-Gorely, (3) Kozelsky-Avacha-Koryaksky-Arik-Aag, and (4) Zhupanovsky-Dzenzur-Bakening. It is interesting that the configurations of the trench-parallel and trench-perpendicular lineaments look symmetrical with respect to the MPZ.

Between Vilyuchinsky Volcano and Avacha Group, there is a gap of ~60 km width, coinciding with the MPZ, where no large stratovolcanoes are observed. At the same time, many manifestations of monogenic volcanism and little extrusions are observed in this area³³. For example, a chain of cinder cones with ages ranging from 2.4 to 10 ka is identified in the valley of the Paratunka River at the southern border of the MPZ³⁴. In the northeastern part of the MPZ, an extrusive dome of Mishennaya Sopka in the Petropavlovsk-Kamchatsky City and other similar structures are dated between 400 and 800 ka³⁵. However, most of them were covered by debris avalanches of the Avacha Volcano eruption that occurred 30 ka BP^{3,36}. The small monogenic volcanic structures within MPZ were presumed to be originated due to decompression melting in the mantle wedge possibly caused by tearing of the slab below the MPZ³³.

Data and algorithms

In this study, we used the data of the temporary network deployed in Central Kamchatka in 2019–2020 supplemented by permanent stations of KBGS located in the same area (red and blue triangles in Fig. 2, respectively). The temporary network initially included 33 stations provided by several institutions of Russia and Taiwan; however, some of them were destroyed by animals and got out of order due to other natural factors. The stations that were used for picking are highlighted with green contour in Fig. 2. The temporary seismic network was composed of broadband seismic instruments of different types including Gularp 6T(D), Thrillium Compact 120 s and Meridian Compact MC120-PH2, which were suitable for recording low-frequency waves from teleseismic sources.

For this study, we used a list of earthquakes from the global ISC catalog³⁷ for the time when the temporary seismic network operated. We selected the data from events located at distances from 15° to 100° from the

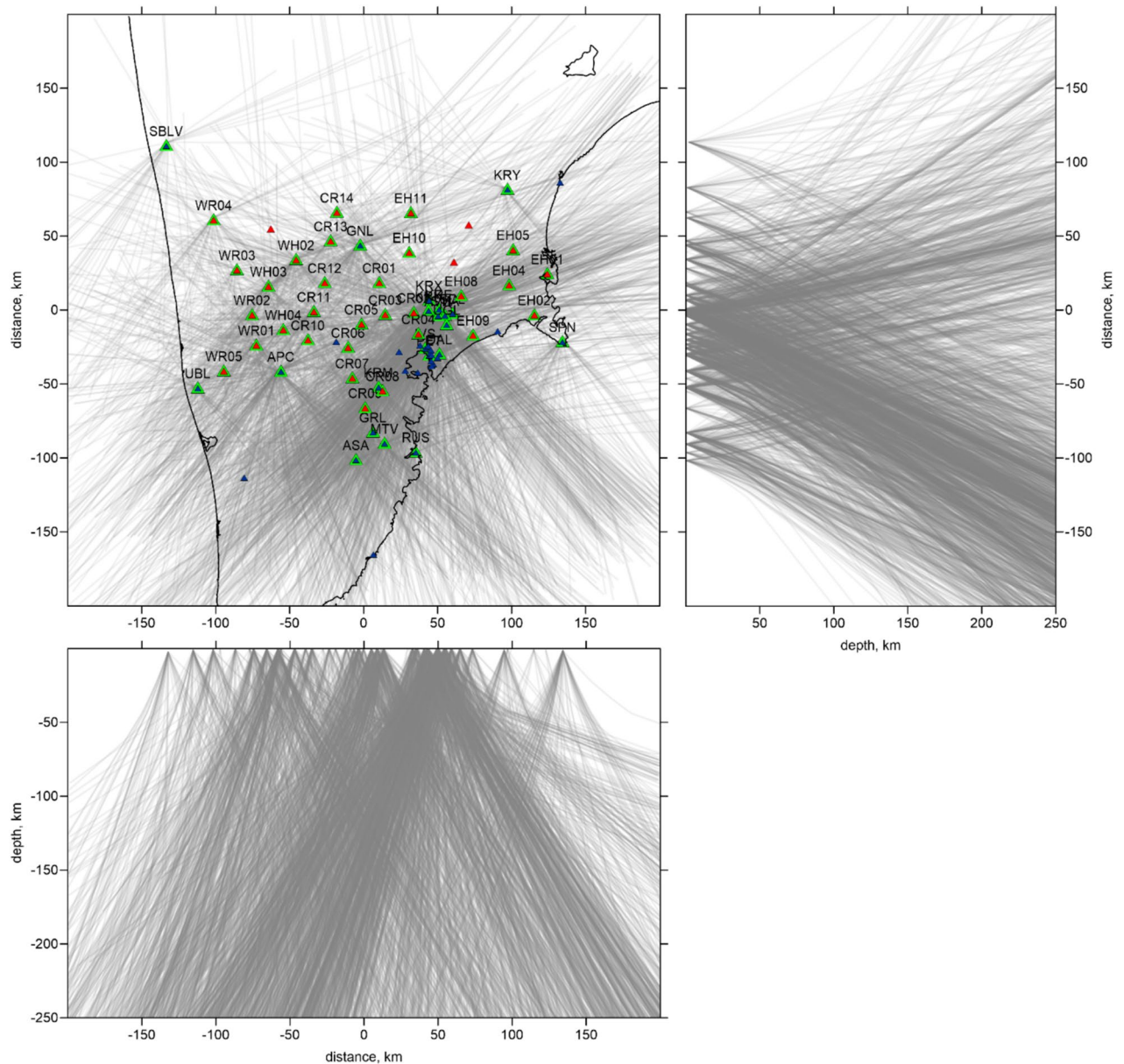


Fig. 2. Ray paths in map view and vertical projections. The triangles in the map indicate seismic stations. Red and green filling of the triangles indicate temporary and permanent stations, respectively; the green contour means that this station is used for the teleseismic data analysis. The figure was generated using the software Surfer (version 13, <http://www.goldensoftware.com/products/surfer>).

center of the network (Fig. 3). The lower limit of this interval is smaller than used in most of other teleseismic studies, where the shortest distance was set at 30° . We believe that adding data from the interval from 15° to 30° is important for two reasons. First, it allows adding weaker events, which would be hardly detectable at distances of more than 30° . Second, the waves from events at shorter distances arrive to the study area along shallower ray paths, which improves the variety of ray geometry in the study area and is favorable for the tomographic inversion. On the other hand, there might be a concern that travel times from events at shorter distances corresponding to shallower ray paths may be perturbed by structures located outside the study area, which may create some artefacts in the resulting model. In this study, we will present several tests that are specially designed to investigate this problem.

To optimize the manual picking procedure and to enable most homogeneous data coverage, we carefully selected the events according to their magnitude and azimuthal distributions. We defined a linearly increasing magnitude threshold depending on epicentral distances, which allowed selections of weaker events at smaller distances and only strong events at larger distances. Then along each azimuthal segment of 1° -degree size, we selected no more than three events with largest magnitudes. As a result of selection, we obtained 473 events.

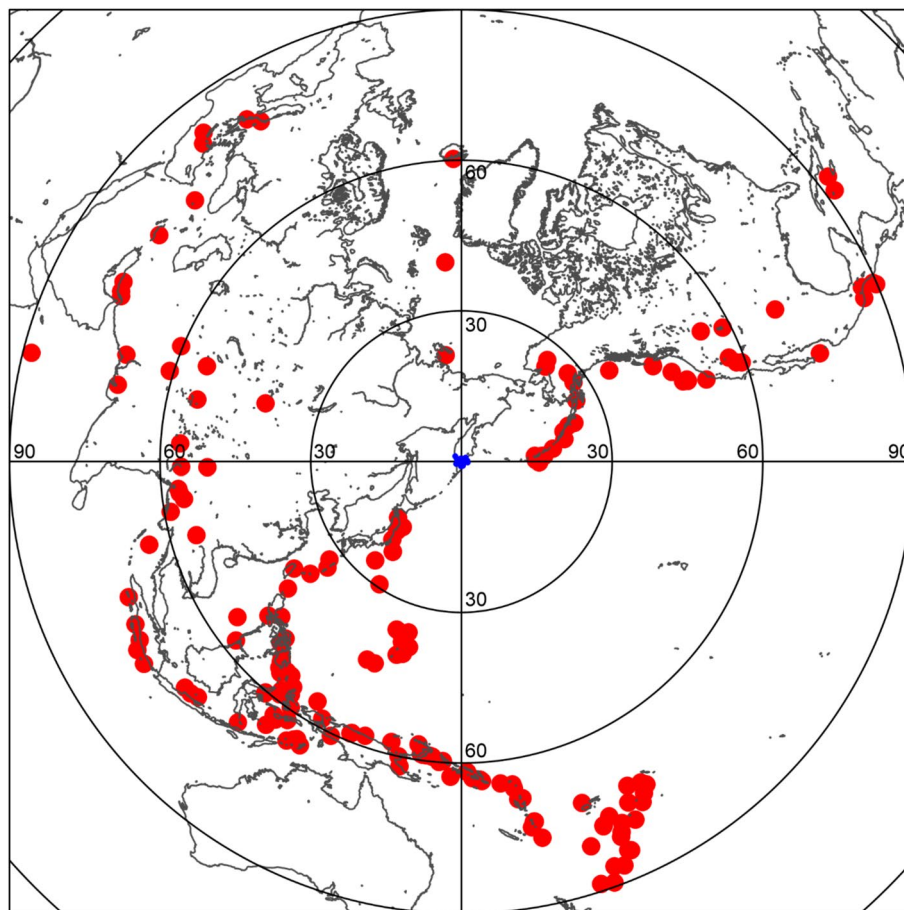


Fig. 3. The distribution of teleseismic events (red dots) used for tomography. The blue dots in the center indicate seismic stations. The figure was generated using the software Surfer (version 13, <http://www.goldensofware.com/products/surfer>).

To pick the arrival times of seismic waves from teleseismic events, we used the SEISAN software³⁸. Figure 4 presents a typical waveform corresponding to a moderate teleseismic event with the magnitude of 5.5 at a distance of approximately 70°. At the initial seismogram shown in the left plot, this event is not visible. After applying several bandpass filters, we selected the frequency range from 1 to 5 Hz, which provided the clearest arrival phases. However, the quality of seismograms for this and most of other events was not good enough to perform automated picking using cross-correlation of waveforms. Therefore, we visually inspected all the waveforms, selected most appropriate filter for each event and manually picked all the phases. When selecting data for tomography, we took into consideration only events for which we could robustly determine 10 or more picks. In total, after this selection criterion, we picked 268 events with corresponding 5894 P-wave arrivals (on average, more than 22 picks per event). The events selected for tomography are shown in Fig. 3. It can be seen that an only gap of approximately 60° exists in the southeastern direction; the other directions are relatively well illuminated.

The travel time differences were calculated with respect to the reference travel time calculated in the model IASP91³⁹. Then the residuals for each event were shifted to enable zero sum of all residuals. If the maximum residual was larger than a predefined threshold (2 s) it was removed, and then the residuals were calculated with respect to a new average value.

For the tomographic inversion, we used a classical approach of K. Aki, A. Christoffersson and E. Husebye (ACH)⁴⁰. The teleseismic tomography is based on an assumption that the measured residuals along the rays from remote events are caused by the seismic velocity anomalies in the study area; outside, the velocity distribution is presumed to be one-dimensional. Similar approach was used in a number of other studies based on teleseismic travel time tomography^{41–43}.

The study area was parameterized in an area with the size of 400 × 400 × 250 km using uniform cells with the size of 6 × 6 × 6 km. In total, it gives 188,539 unknown parameters describing the velocity distribution. The first derivative matrix was calculated along the ray paths that were constructed analytically in the 1D spherical velocity model IASP91³⁹. To stabilize the solution of the linear equation system, we supplemented it with additional equations having two elements of opposite signs corresponding to all combinations of neighboring cells and zero data vector. Increasing the weights of these equations (W^{sm}) smoothens the resulting velocity anomalies. Since the cell size is far below the resolution of the model, and the stability is merely determined by

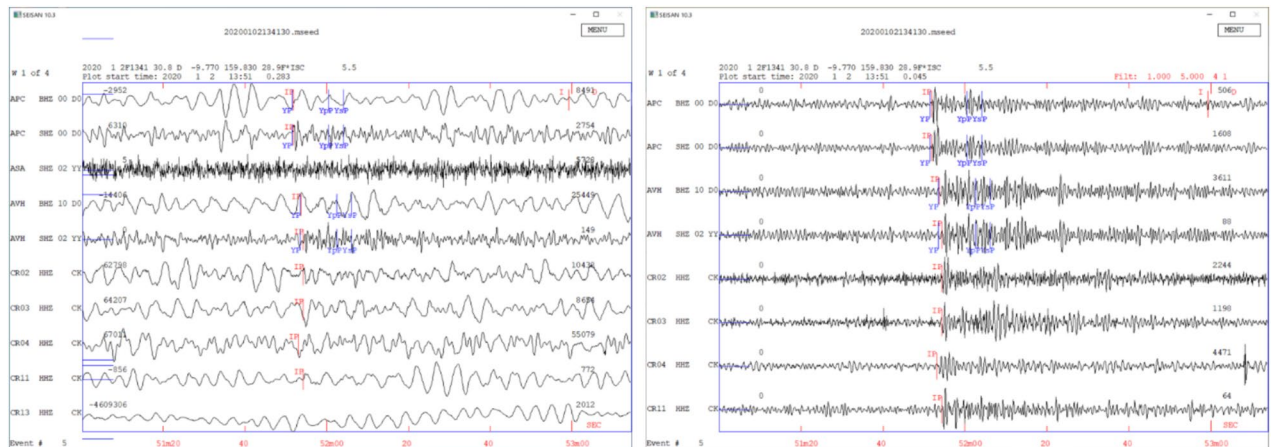


Fig. 4. A screenshot of the SEISAN software⁶⁰ with an example of picking an event with the magnitude of 5.5 located at a distance of $\sim 70^\circ$. The left panel shows the initial seismogram without filtering, in which the arrival wave is almost not visible. The right panel shows the result of the bandpass filtering in the frequency range of 1–5 Hz, which was found most appropriate in this case. The blue indications highlight theoretical phases, and the red ones indicate the manual picking results.

the smoothing value, this type of parameterization is quasi-continuous and almost not dependent on the cell geometry. The smoothness coefficients in inversion were defined depth dependent: at the surface the $W^{sm} = 30$, at 250 km depth $W^{sm} = 150$, and in between it was linearly interpolated. Furthermore, we defined an amplitude damping presuming adding equations with only one non-zero element with the value W^{am} corresponding to each cell (in our case, $W^{am} = 20$). In addition, we determined an additional correction for each event that allowed us to shift the time residual, which includes all the factors affecting the ray tube between the source point and the bottom of the study area. All values of these controlling parameters were obtained after several trials during inversions of experimental and synthetic data. The best values aimed at avoiding oversmoothed and patchy solutions in the case of experimental data, and provided the best recovery of models in synthetic tests. In total we got a system with 747,728 equations that was inverted using the Least Square method with QR factorization (LSQR)^{44,45}.

Synthetic modeling

Prior to considering the results of experimental data inversion, we present the results of synthetic tests that provide the information about the spatial resolution of the resulting model. To calculate the synthetic data, we used the actual geometry of the ray paths corresponding to the data in the main model. Note that at this step, we considered the entire ray paths between sources and receivers. This gives a possibility to explore the effect of anomalies located outside the study area. The synthetic times were perturbed with random noise with a Gaussian statistical distribution. In all tests presented here, we used noise with the mean value of 0.3 s in L1 norm. To recover the model in the study area, we repeated the same inversion procedure and used the same controlling parameters as in the case of computing the main tomography model.

In the first series of tests presented in Fig. 5, we defined the three-dimensional checkerboard model with cubic anomalies of 50 km size and 15 km of empty intervals in x, y and z directions and anomaly values of $\pm 10\%$. In the first trial, we defined the checkerboard patterns only within the area, in which we performed inversion (upper two rows in Fig. 5). The results of the recovery are shown in two horizontal and two vertical sections; the initial synthetic anomalies are highlighted with dotted lines. It can be seen that at least three layers of alternated anomalies are correctly recovered in areas with sufficient station coverage. At a depth of 150 km, the area of the best resolution is shifted to the south, where most of the rays are directed. In the vertical sections, we can observe fair resolution of the anomalies below the central part of the model. However, at large depths in the marginal parts, we observe some diagonal smearing mostly caused by dominant orientations of the ray paths. This type of artifacts should be considered while interpreting the results of experimental data inversion.

In this study, we used a non-traditional ray configuration with shorter epicentral distances than usually considered in teleseismic tomography, which presumes that some rays cross not only the bottom, but also side limits of the study area. This causes some concerns that anomalies located outside the study area in neighboring regions may affect the resulting model. To address this concern, in the next test shown in two lower lines in Fig. 5, we considered the checkerboard model that took into account the anomalies located outside the study area. In this case, we created a model with the same geometry of anomalies as in the previous test, but defined in a cube of $770 \times 770 \times 700$ km, which is much larger than the size of the study area ($400 \times 400 \times 250$ km). When computing the synthetic travel times, we integrated along the entire ray path and accumulated the contributions of anomalies located both inside and outside the study area. Then we carried out the tomography inversion merely within the study area. It can be seen that in this case, the main recovered patterns can be observed in correct locations, but look more disturbed than in the previous test. This means that the outside anomalies affect

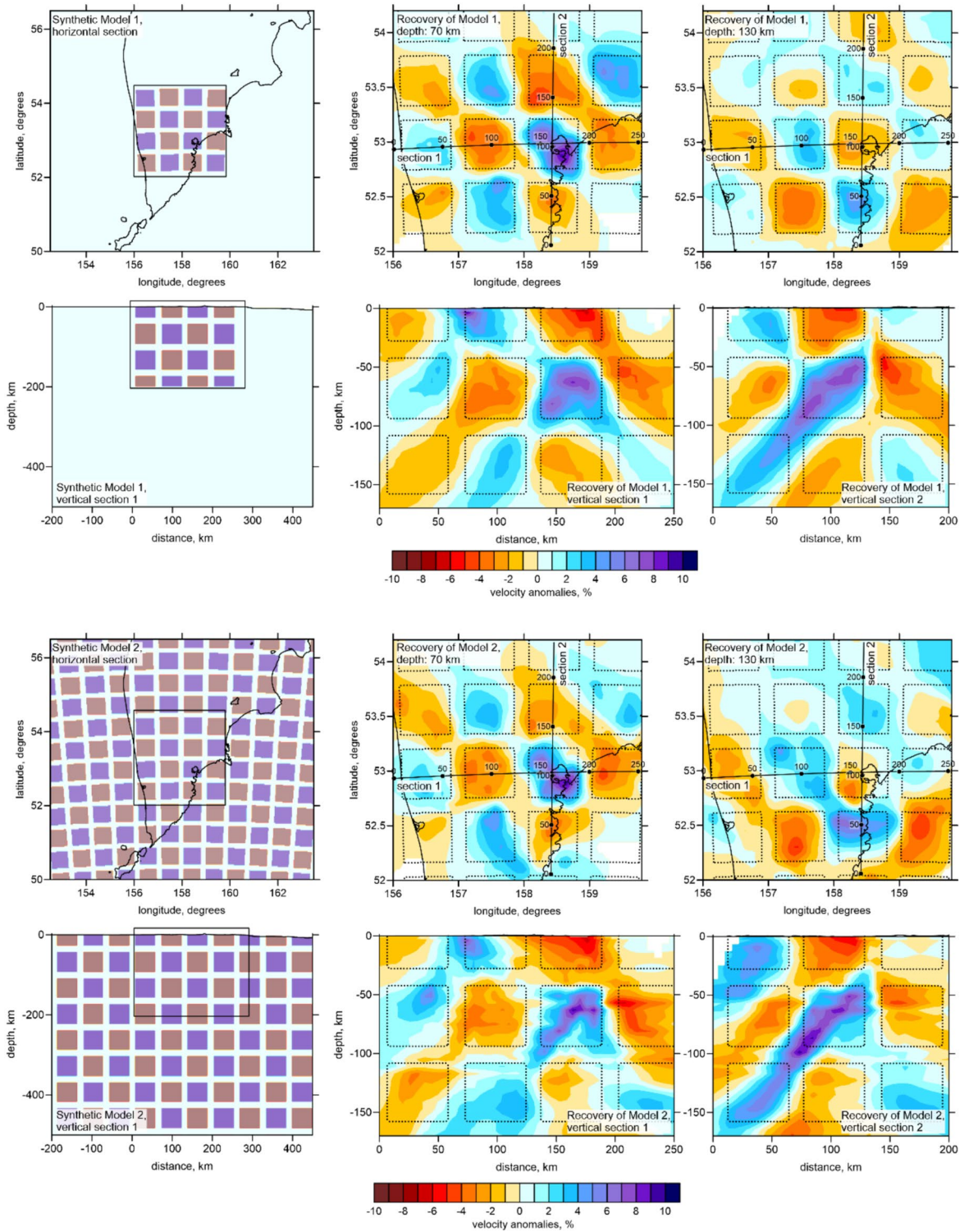


Fig. 5. Results of two checkerboard tests showing the effect of anomalies located outside the resolved area. The upper two lines present the test for the Model 1, in which the synthetic anomalies are defined in the investigated area only, and the lower two lines show the test for the Model 2 with an unlimited checkerboard model. The left column presents the synthetic models on a larger scale in horizontal and vertical sections. Rectangles indicate the limits of the study area. The 2nd and 3rd columns present the recovery results in two horizontal and two vertical sections. In the resulting images, the shapes of the initial synthetic patterns are highlighted with the dotted lines. The locations of the sections are shown in the maps. The figure was generated using the software Surfer (version 13, <http://www.goldensoftware.com/products/surfer>).

the data as noise that does not create a considerable large-scale coherent contributions in the space of the model, but only produces smaller-scale perturbations.

One may state that this checkerboard test is not totally adequate to estimate the contribution of outside anomalies, because the alternated positive and negative anomalies in a large volume compensate effects of each other, and in total do not create biased patterns in distributions of the residuals. To answer such a potential criticism, we have created a series of synthetic models with free-shaped anomalies shown in Fig. 6. In these cases, the anomalies were defined by a set of polygons in the vertical section oriented across the subduction zone. In Model 1, we defined a large mushroom-shaped low-velocity mantle upwelling and several high-velocity patterns

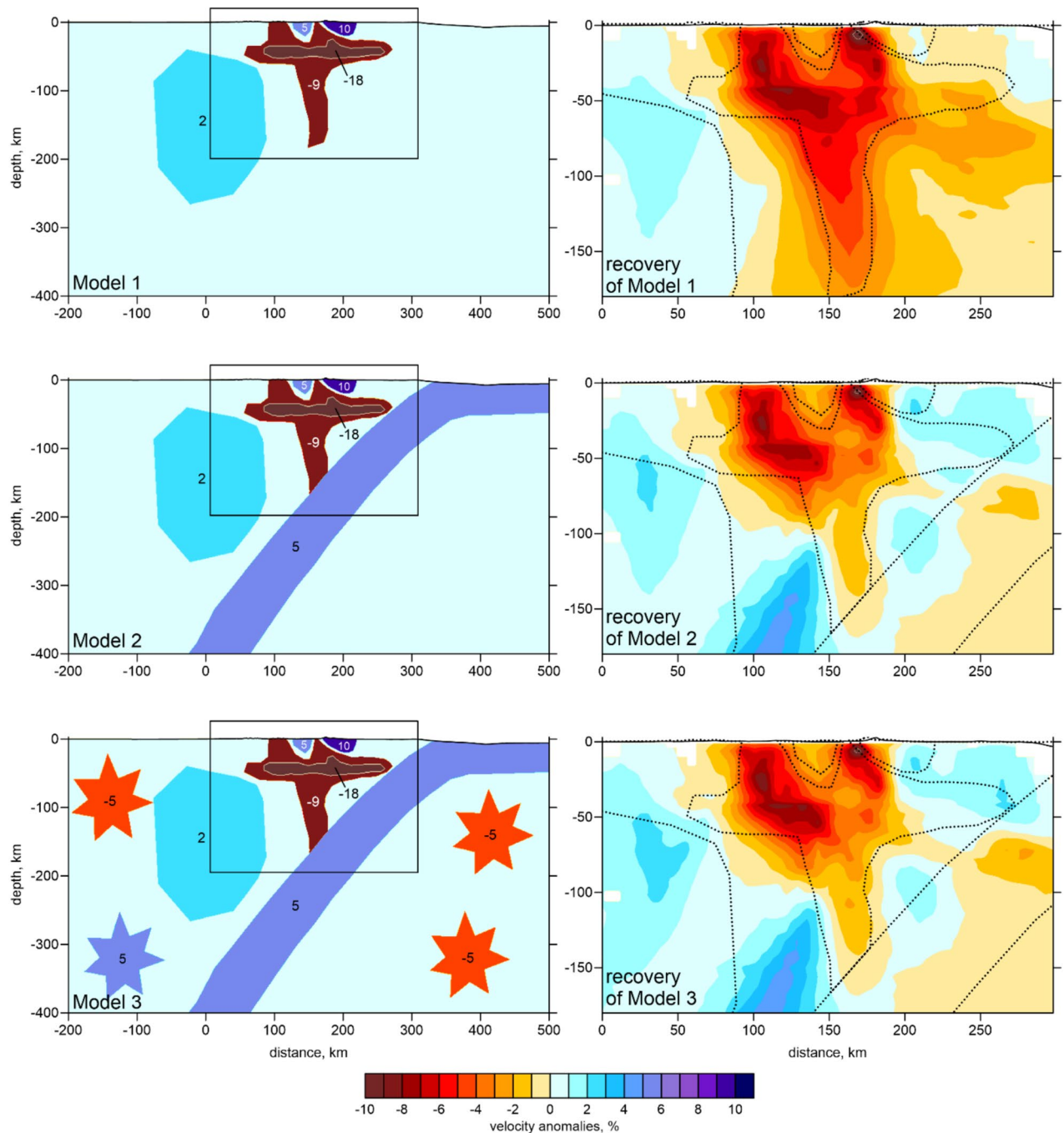


Fig. 6. Synthetic tests for three free-shaped models defined in the vertical section 1 (same as in Fig. 8). The left column presents the initial synthetic model in the same section, but on a larger scale, and the right column presents the recovery results for the corresponding models. The numbers indicate the values of the synthetic anomalies in percent. The dotted lines in the resulting images highlight the shapes of the synthetic anomalies. The rectangles in the left column highlight the limits of the study area. The figure was generated using the software Surfer (version 13, <http://www.goldensoftware.com/products/surfer>).

representing crustal and mantle structures discovered in the main model. In Model 2, to all the same anomalies as in Model 1, we have added a high-velocity slab. In Model 3, we supplemented Model 2 with four additional fancy stars of different signs located outside the study area.

The recovery results show that in all cases, the main contours of the central low-velocity anomaly are generally well recovered, whereas for the shallow high-velocity patterns, we only observe some local reduction of the low-velocity anomaly intensity. For Models 2 and 3, we can see that the inversion cannot recover the slab in its correct limits. We only obtain some weak high-velocity anomaly above the upper part of the slab and stronger high-velocity anomaly above its lower part. This result demonstrates that we cannot expect clear images of the slab in our tomography results due to unfavorable ray geometry. Finally, we do not observe any difference between the recovery results of Models 2 and 3. It means that the external stars do not have any contribution into the teleseismic tomography results. Based on the results of synthetic tests shown in Figs. 5 and 6, we can conclude that in the case of our ray configuration, the anomalies located outside the study area have a minor effect on the tomography result.

Velocity model and interpretation

The resulting anomalies are visualized in a set of horizontal and vertical sections (Figs. 7, 8). Schematic interpretation of the result in one of the vertical sections is presented in Fig. 9. When preparing visualization of the results, we calculated the 3D distribution of the ray density (total length of rays in each cubic cell with the size of 6 km) and then smoothed it. In sections, we show the results only if the ray density is larger than 5% of the average value; otherwise, the areas with insufficient ray coverage are blanked. According to the resolution tests, the resolved area in vertical sections has a shape of an inverted triangle with the upper size coinciding with the network area and the bottom point at approximately 150 km depth (dotted line in Fig. 9). Outside this triangle, the anomalies may be smeared and should be considered with prudence.

This model can be compared with the results obtained in other studies for the same region including the tomography models by Bushenkova et al.¹⁹, which was based on body waves from the local earthquake tomography (LET), and by Egorushkin et al.²⁰ based on ambient noise tomography (ANT). There is some similarity of our results with the LET model at the depth of 20 km. In particular, a low-velocity anomaly between Gorely, Mutnovsky and Viluchinsky volcanoes looks very similar in both models. Similar low-velocity anomalies at 20 km depth are also identified in areas of Shipunsky Cape and Sredinny Ridge. Higher-velocity structures in both models are associated with the Avacha Graben and Ganalsky Ridge. Similar patterns are identified in our model and in the ANT model for the depths of 20 and 40 km in the area of the Avacha group of volcanoes. Some similarity between our and LET models is also observed at a depth of 60 km, where a large low-velocity anomaly dominates in the central part of the study area in the both models, except for the Nalychev Valley, for which opposite signs of anomalies were identified. Note that the consistent positive anomalies below the Nalychevo Valley at 40 km depth are observed in our and ANT models.

We admit that the total amount of data in Bushenkova et al.¹⁹ was much larger than in our study. However, the workflow used in that study had several issues that may disturb their model. In particular, most of events in their study were located below the Pacific Ocean at one side of the network. This does not provide good ray crossing at mantle depths below the network, which limits the resolution of tomography for the mantle wedge. Furthermore, joint inversion for the source locations and velocity distributions gives some trade-off between these parameters for the deep and out-of-network events, which may cause some artefacts in the velocity model. In our model, the data distribution is more homogeneous and the residuals used in teleseismic tomography are not coupled with source hypocenter coordinates, which makes the inversion more stable compared to the LET tomography. Our model reveals some important patterns that can be used for interpretation in terms of geological processes.

In the mantle depths, the most prominent structure is a large low-velocity anomaly that is seen in the center of the study area below the depth of 40–50 km. In map view, we see that this anomaly roughly corresponds to the Avacha Graben and Malko-Petropavlovsk Zone of transverse dislocations (MPZ). According to some authors, MPZ is located at a continuation of the Avacha transform fault in the oceanic Pacific Plate separating two segments with different ages and properties and possibly coinciding with slab tear^{27,28}. Of course, our model cannot reveal the fact of the slab tear because of insufficient resolution, and we can only hypothesize about it from indirect observations³³. In this case, the observed prominent low-velocity anomaly below MPZ might represent overheated asthenospheric material in the mantle wedge that ascended through the slab window (red arrows in Fig. 9). This hypothesis is supported by a relatively high heat flow within MPZ compared to the surrounding areas³². The typical magma generation zone of frontal volcanoes is approximately 120 km above the slab²⁸. However, the recorded low-velocity anomaly from depths greater than 150 km (Fig. 8, section 3, 4) indicates that the phenomenon can be attributed to a slab window rather than mantle heterogeneity. Furthermore, the distribution of monogenetic cones does not correspond to the main magma generation zone and does not exhibit a correlation with distance to the trench³³. The isotopic and petrological investigation of the large-voluminous (~800 km³) Karymshina caldera suggests the formation of rising basalts in the upper crust, which subsequently melted the surrounding crust and gave rise to a series of strong eruptions between 4 and 0.5 Ma⁴⁶.

At crustal depths (in a section at 20 km), above the mantle low-velocity anomaly, we observe a dominating high-velocity anomaly within the MPZ. This high-velocity structure might represent a rigid crustal block that prevents the propagation of the hot material from the mantle wedge to the surface. We see that this area of MPZ corresponds to a clear gap in the distribution of large stratovolcanoes and volcanic complexes, as highlighted in Fig. 1A. The rigid properties of the crust in this location can also be proven by a relatively flat topography in this area, which was initially affected by regional tectonic stresses, but could not be deformed due to high rigidity. On the other hand, within MPZ, we observe a series of relatively small monogenetic cones³³ that mostly match with the high-velocity anomaly in the crust and low-velocity in the mantle wedge. We can propose that the rigid block

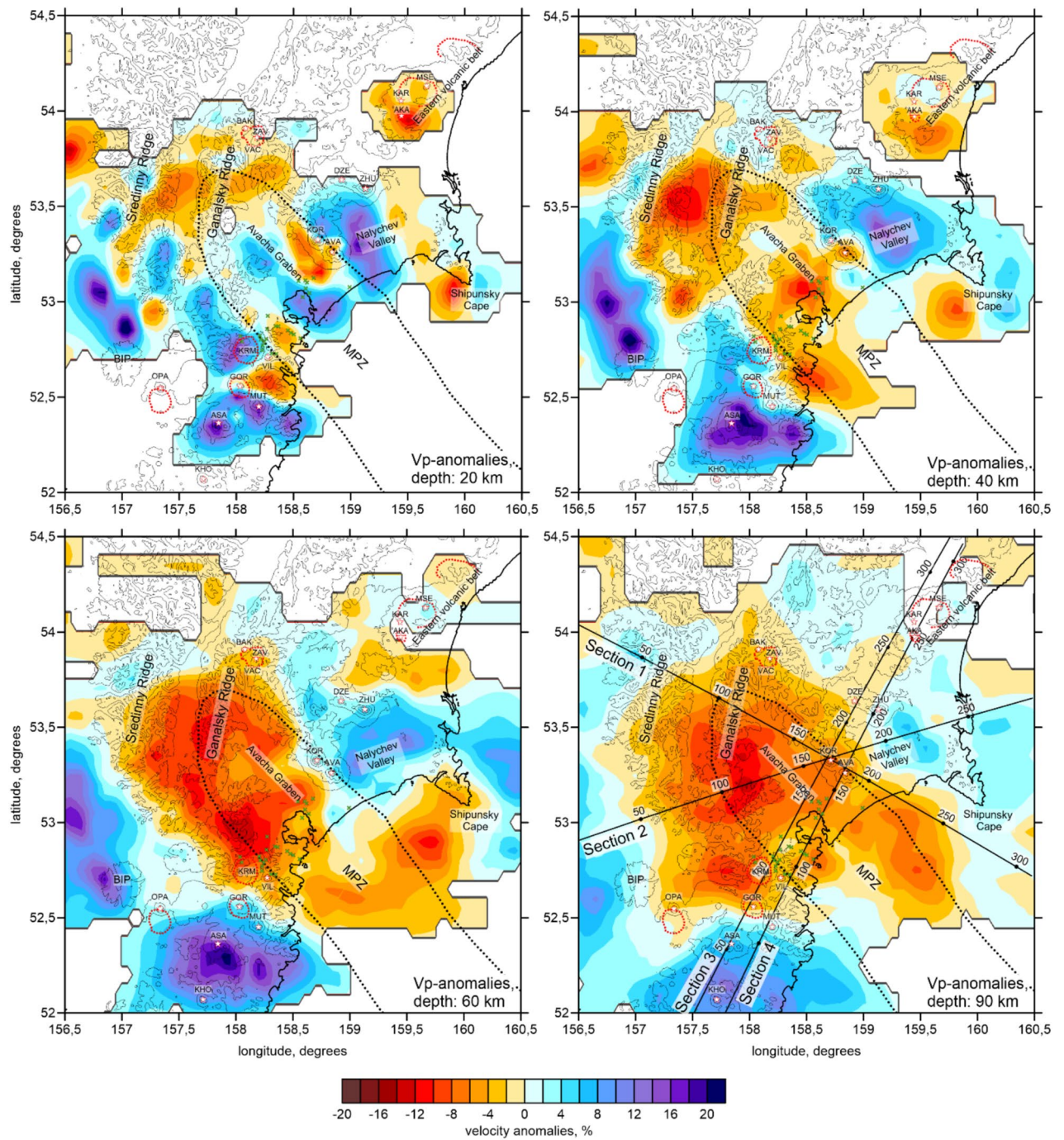


Fig. 7. Resulting anomalies of the P-wave velocity in horizontal sections. The thin contour lines indicate the topography with the interval of 500 m. The black dotted line highlights the Malko-Petropavlovsk fracture zone (MPZ). The red dotted line highlights major calderas. The red crosses indicate monogenic cones within the Avacha Graben. PKC—Petropav-lovsk—Kamchatsky City. Abbreviations for volcanoes: KHO—Khodutka, ASA—Asacha; OPA—Opala; BIP—Bolshaya Ipelka; MUT—Mutnovsky; Gor—Gorely; VIL—Vilyuchinsky, KAR—Karymshina Caldera; KOR—Koryaksky; AVA—Avachinsky; DZE—Dzenzur; Zhu—Zhupanovsky; VAC—Verkhnevavchinskaya Caldera; ZAV—Zavaritskogo; BAK—Bakening; AKA—Akademii Nauk; KAR—Karymsky; MSE—Maly Semyachik. The figure was generated using the software Surfer (version 13, <http://www.goldensoftware.com/products/surfer>).

of the MPZ behaves in a brittle way. In a case of excessive pressure on its bottom, a system of hydro-fractures (thin black lines in Fig. 9) may quickly form and bring low-viscous basaltic magma to the surface to produce a single eruption episode that formed a monogenic cone (red triangles in Fig. 9). However, in such conditions, no large intercrustal magma reservoirs can be formed that could feed long-term activity of large stratovolcanoes.

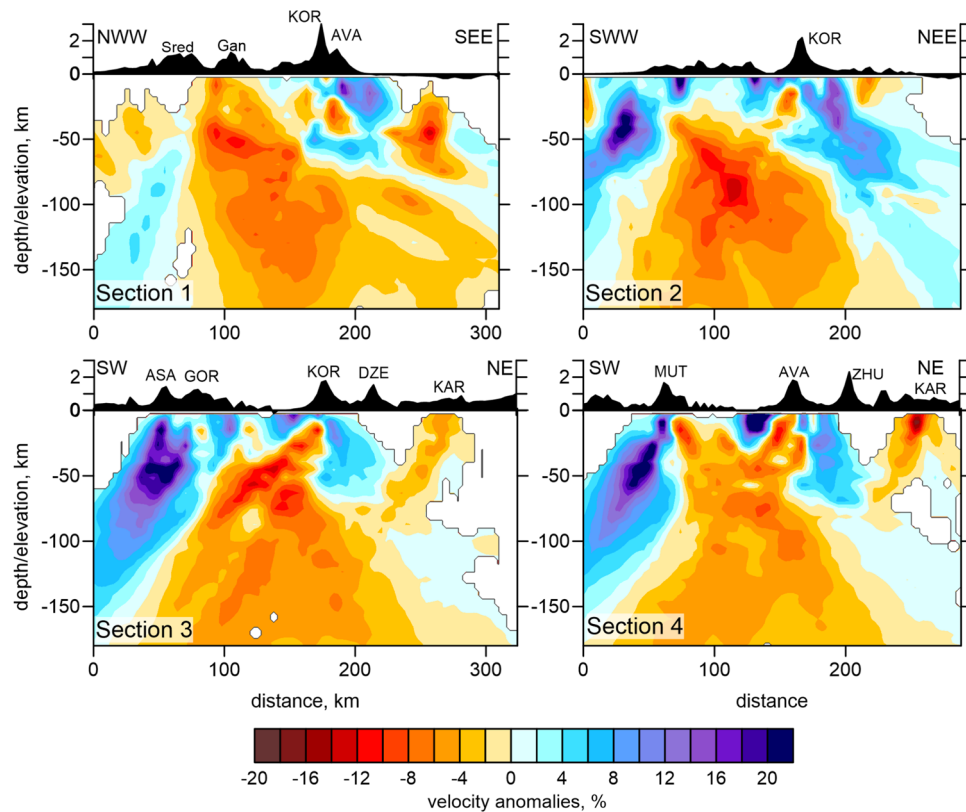


Fig. 8. Resulting anomalies of the P-wave velocity in four vertical sections. Exaggerated relief is presented above each section. The locations of the sections are shown in Fig. 7 in the map at 90 km depth. Abbreviations for the mountain ranges: Sred—Sredinny; Gan—Ganalsky. Abbreviations for volcanoes: AVA—Avachinsky; KOR—Koryaksky; ASA—Asacha; GOR—Gorely; MUT—Mutnovsky; ZHU—Zhupanovsky; DZE—Dzhenzur; KAR—Karymsky. The figure was generated using the software Surfer (version 13, <http://www.goldensoftware.com/products/surfer>).

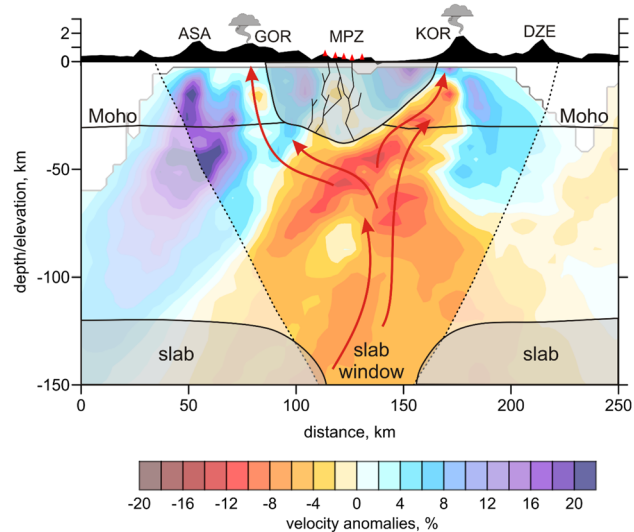


Fig. 9. Schematic interpretation of the resulting anomalies of P-wave velocity in section “Data and algorithms”. The red triangles depict the distributed monogenic cones. The area with the dotted line contour masks the low-resolution parts of the model. The red arrows indicate possible flows of hot material from the slab window. Abbreviations: KOR—Koryaksky Volcano; ASA—Asacha Volcano; GOR—Gorely Volcano; DZE—Dzhenzur Volcano; MPZ—Malko-Petropavlovsk Fracture Zone. “Smokes” above GOR and KOR indicate that they are active volcanoes. The figure was generated using the software Surfer (version 13, <http://www.goldensoftware.com/products/surfer>).

Avacha and Koryaksky volcanoes appears to be located at the border between the low and high-velocity anomalies. The local low-velocity anomaly at 20 km depth to the southwest of Avacha and Koryaksky volcanoes corresponds to a prominent low-density anomaly inferred from the gravity inversion⁷. Similar pattern was identified based on the inversion of more than 1000 of magnetotelluric measurements showing low resistivity to the southwest of Avacha and high resistivity to the northeast⁸. Although the active-source seismic survey covered much shallower depth intervals, it demonstrates the same feature: low velocity to the southwest of Avacha and high velocity to the northeast^{9–11}. Same feature is identified from the ambient noise tomography studies on a local-scale¹¹ and on a regional-scale²⁰. This feature can be explained by weaker mechanical properties of suture zones between different geological formations that make easier propagation of fluids and melts along such contacts.

On the other side of the MPZ, Viluchinsky, Mutnovsky and Gorely volcanoes are also located close to the contact zone between low- and high-velocity zones. This presumes a similar mechanism of feeding these volcanoes from the mantle sources as in the case of Avacha and Koryaksky volcanoes. As we see in sections 3 and 4 in Figs. 8 and 9, a large low-velocity anomaly below MPZ may represent ascending hot material that reached the bottom of the crust and propagate along it to the borders of the block, where it ascends to the surface and form large complexes of stratovolcanoes.

The clustering of volcanoes such as Kozelsky-Avacha-Koryaksky volcanoes and Mutnovsky-Gorely volcanoes are low-velocity areas, formed perpendicular to the trench (Figs. 1, 8). These observations are similar to those made and called as a finger-like volcano chain in Northern Japan, where these volcanoes were also formed as hot regions in the mantle wedge⁴⁷.

To the northeast of the Avacha Group, we observe the high-velocity anomaly coinciding with the Nalychevo valley. This valley is nearly flat and tectonically not strongly deformed, which may indicate that it also corresponds to another rigid crustal block. Some observed manifestations of active geothermal activity in the Nalychevo Valley⁴⁸ may be caused by lateral migration of fluids in the crust from active volcanoes of the Avacha and Zhupanovsky groups, and are probably not related to direct heating by deep sources in the mantle wedge, which appears to be not sufficiently hot.

Unfortunately, we did not have seismic stations in the area of Zhupanovsky and Dzenzur volcanoes, therefore we have a gap in our tomography at crustal depths. At the same time, if we extrapolate deeper structures, we can propose that these volcanoes might be also located at a contact between high- and low-velocity anomalies. We also see some low-velocity anomalies between Karymsky Volcano, but for this area, we have too little data, therefore, we should be prudent to this result.

Conclusions

Based on the data of a temporary seismic network and permanent stations, we have obtained a new model of the P-wave velocity anomalies for the mantle wedge and crust beneath central Kamchatka, where several large active volcanic centers are located.

In the mantle, we observe a large low-velocity anomaly coinciding with the location of the MPZ. We propose that this anomaly represents hot material that was ascended through the slab window at a continuation of a transform fault on the Pacific Plate. At crustal depths, the area of Avacha graben is associated with dominated high velocity anomalies that may represent the presence of a rigid block. In this case, it prevents the origin of large crustal magma chambers, and therefore, in this area we observe a gap in the distribution of large arc stratovolcanoes. At the opposite borders of the mantle low-velocity anomaly, we observe two symmetrical pairs of active volcanic systems: Avacha—Koryaksky to the northeast and Gorely—Mutnovsky to the southwest. We propose that the hot material surrounds the bottom of the rigid crustal block of the Avacha Graben, follows weakened zones along its borders and when reaching the surface, it causes the formation of active volcanoes.

Data availability

No datasets were generated or analysed during the current study.

Received: 27 September 2024; Accepted: 5 May 2025

Published online: 14 May 2025

References

- DeMets, C., Gordon, R. G., Argus, D. F. & Stein, S. Current plate motions. *Geophys. J. Int.* **101**(2), 425–478 (1990).
- Holocene Kamchatka volcanoes. <http://www.kscnet.ru/ivs/volcanoes/holocene/main/main.htm> (2024).
- Melekestsev, I. V., Litasova, S. N. & Sulerzhitskii, L. D. The age and scale of catastrophic eruptions of the directed explosion type in the Avacha Volcano (Kamchatka) in the Late Pleistocene. *Volcanol. Seismol.* **13**(2), 135–146 (2009).
- Dobretsov, N. L., Koulakov, I. Y., Litasov, K. D. & Kukarina, E. V. An integrate model of subduction: contributions from geology, experimental petrology, and seismic tomography. *Russ. Geol. Geophys.* **56**(1–2), 13–38 (2015).
- Steinberg, G. S. & Zubin, M. I. The depth of the magmatic focus under the Avachinsky volcano. *Dokl. Akad. Nauk SSSR* **152**(4), 968–971 (1963).
- Masurenkov, Y. P. The composition and state of a matter in the magma chamber of the Avachinsky volcano (Kamchatka). In *Magma of Shallow Depth Chambers* 79–89 (Nauka, 1970).
- Zubin, M. I. & Kozyrev, A. I. Gravity model of the Avachinsky volcano (Kamchatka). *Volcanol. Seismol.* **1**, 81–94 (1988) (in Russian).
- Moroz, Y. F. & Nurmukhamedov, A. G. Magnetotelluric sounding in the Petropavlovsk geodynamic test site. *Volcanol. Seismol.* **2**, 77–84 (1998).
- Balesta, S. T., Gontovaya, L. I., Kargopol'tsev, A. A., Pushkarev, V. G. & Senyukov, S. L. Seismic model of the Avacha volcano. *Volcanol. Seismol.* **2**, 43–55 (1988).
- Gontovaya, L. I. & Senyukov, S. L. On seismic model of the Earth's crust beneath the Avachinsky volcano in Kamchatka. *Volcanol. Seismol.* **3**, 57–62 (2000).

11. Koulakov, I. et al. Asymmetric caldera-related structures in the area of the Avacha group of volcanoes in Kamchatka as revealed by ambient noise tomography and deep seismic sounding. *J. Volcanol. Geoth. Res.* **285**, 36–46 (2014).
12. Chebrov, V. N. et al. The system of detailed seismological observations in Kamchatka in. *J. Volcanol. Seismol.* **7**, 16–36 (2013).
13. Gorbатов, A., Fukao, Y., Widiyantoro, S. & Gordeev, E. Seismic evidence for a mantle plume oceanwards of the Kamchatka–Aleutian trench junction. *Geophys. J. Int.* **146**(2), 282–288 (2001).
14. Jiang, G., Zhao, D. & Zhang, G. Seismic tomography of the Pacific slab edge under Kamchatka. *Tectonophysics* **465**(1–4), 190–203 (2009).
15. Koulakov, I. Y., Dobretsov, N. L., Bushenkova, N. A. & Yakovlev, A. V. Slab shape in subduction zones beneath the Kurile–Kamchatka and Aleutian arcs based on regional tomography results. *Russ. Geol. Geophys.* **52**(6), 650–667 (2011).
16. Bushenkova, N. et al. Tomographic images of magma chambers beneath the Avacha and Koryaksky volcanoes in Kamchatka. *J. Geophys. Res. Solid Earth* **124**(9), 9694–9713 (2019).
17. Kitsura, E. et al. Seismic structure beneath the Avacha and Koryaksky volcanoes in Kamchatka based on the data of permanent and temporary networks. *J. Volcanol. Geoth. Res.* **443**, 107937 (2023).
18. Gontovaya, L. I., Popruzhenko, S. V., Nizkous, I. V. & Aprelkov, S. E. Upper mantle beneath Kamchatka: The depth model and its relation to tectonics. *Russ. J. Pac. Geol.* **2**, 165–174 (2008).
19. Bushenkova, N. et al. Connections between arc volcanoes in Central Kamchatka and the subducting slab inferred from local earthquake seismic tomography. *J. Volcanol. Geotherm. Res.* **435**, 107768 (2023).
20. Egorushkin, I. et al. Crustal structure beneath Central Kamchatka inferred from ambient noise tomography. *J. Volcanol. Geotherm. Res.* **449**, 108070 (2024).
21. Lander, A. V. & Shapiro, M. N. The origin of the modern Kamchatka subduction zone. *Geophys. Monogr. Ser.* **172**, 57–64 (2007).
22. Avdeiko, G. P., Palueva, A. A. & Khleborodova, O. A. Geodynamic conditions of volcanism and magma formation in the Kurile–Kamchatka island-arc system. *Petrology* **14**, 230–246 (2006).
23. Vlasov, G. M. Kamchatka, Komandor and Kurile islands. Geology of USSR. XXXI. (Ed.). Nedra, Moscow, 733 (1967).
24. Nurmukhamedov, A. G. & Sidorov, M. D. Deep structure and geothermal potential along the regional profile set from Opala Mountain to Vakhil' River (Southern Kamchatka). *IOP Conf. Ser. Earth Environ. Sci.* **249**(1), 012041 (2019).
25. Sheimovich, V. S. & Sidorov, M. D. Structure of the basement under the southern Kamchatka volcanic belt. *Volcanol. Seismol.* **5**, 28–35 (2000).
26. Moroz, Y. F. & Gontovaya, L. I. Deep structure of South Kamchatka according to geophysical data. *Geodyn. Tectonophysics.* **9**(4), 1147–1161 (2018).
27. Andreev, A. A. Transform faults of the Earth's crust Northwestern Pacific. *Pac. Geol.* **3**, 11–20 (1993).
28. Syracuse, E. M. & Abers, G. A. Global compilation of variations in slab depth beneath arc volcanoes and implications. *Geochem. Geophys. Geosyst.* <https://doi.org/10.1029/2005GC001045> (2006).
29. Agibalov, A. O., Bergal-Kuvikas, O. V., Zaitsev, V. A., Makeev, V. M. & Sentsov, A. A. Relation between morphometric parameters of relief characterizing the fracturing of the upper part of the lithosphere and manifestations of volcanism in the Malko-Petropavlovsk Zone. *Izv. Atmos. Ocean. Phys.* **59**(8), 971–981 (2023).
30. Gordeev, E. I. & Bergal-Kuvikas, O. V. Structure of the subduction zone and volcanism in Kamchatka. *Dokl. Earth Sci.* **502**(1), 21–24 (2022).
31. Levina, V. I., Lander, A. V., Mityushkina, S. V. & Chebrova, A. Y. The seismicity of the Kamchatka region: 1962–2011. *J. Volcanol. Seismol.* **7**, 37–57 (2013).
32. Sugrobov, V. M. & Yanovsky, F. A. Geothermal field of Kamchatka, heat losses by volcanoes and hydrotherms. In *Active Volcanoes of Kamchatka* (eds Fedotov, S. A., & Masurenkov, Yu. P.) 67–74 (1991).
33. Bergal-Kuvikas, O. et al. Pleistocene-Holocene monogenic volcanism at the Malko-Petropavlovsk zone of transverse dislocations on Kamchatka: Geochemical features and genesis. *Pure Appl. Geophys.* **179**(11), 3989–4011 (2022).
34. Dirksen, O. V. Late quaternary areal volcanism of Kamchatka. Doctoral dissertation, Sankt-Petersburg State University, 171 (2009).
35. Sheimovich, V. S., Golovin, D. I. & Gertsev, D. O. The andesite extrusion of Mount Mishennaya, Kamchatka, and its age. *J. Volcanol. Seismol.* **1**(4), 248–253 (2007).
36. Braitseva, O. A. et al. Tephra of the largest prehistoric Holocene volcanic eruptions in Kamchatka. *Quatern. Int.* **13**, 177–180. [https://doi.org/10.1016/1040-6182\(92\)90025-W](https://doi.org/10.1016/1040-6182(92)90025-W) (1992).
37. International Seismological Centre, On-line Bulletin. <https://doi.org/10.31905/D808B830> (2022).
38. Havskov, J. & Ottemoller, L. SEISAN earthquake analysis software. *Seismol. Res. Lett.* **70**(5), 532–534 (1999).
39. Kennett, B. L. N. & Engdahl, E. R. Traveltimes for global earthquake location and phase identification. *Geophys. J. Int.* **105**(2), 429–465 (1991).
40. Aki, K., Christofferson, A. & Husebye, E. S. Determination of the three-dimensional seismic structure of the lithosphere. *J. Geophys. Res.* **82**(2), 277–296 (1977).
41. Achauer, U. A study of the Kenya rift using delay-time tomography analysis and gravity modelling. *Tectonophysics* **209**(1–4), 197–207 (1992).
42. VanDecar, J. C., James, D. E. & Assumpção, M. Seismic evidence for a fossil mantle plume beneath South America and implications for plate driving forces. *Nature* **378**(6552), 25–31 (1995).
43. Koulakov, I. et al. Teleseismic tomography reveals no signature of the Dead Sea Transform in the upper mantle structure. *Earth Planet. Sci. Lett.* **252**(1–2), 189–200 (2006).
44. Paige, C. C. & Saunders, M. A. LSQR: An algorithm for sparse linear equations and sparse least squares. *ACM Trans. Math. Softw.* **8**(1), 43–71 (1982).
45. Nolet, G. Seismic wave propagation and seismic tomography. In *Seismic Tomography: With Applications in Global Seismology and Exploration Geophysics*, 1–23 (Springer, 1987).
46. Bindeman, I. N., Anikin, L. P. & Schmitt, A. K. Archean xenocrysts in modern volcanic rocks from Kamchatka: Insight into the basement and paleodrainage. *J. Geol.* **124**(2), 247–253 (2016).
47. Tamura, Y., Tatsumi, Y., Zhao, D., Kido, Y. & Shukuno, H. Hot fingers in the mantle wedge: new insights into magma genesis in subduction zones. *Earth Planet. Sci. Lett.* **197**(1–2), 105–116 (2002).
48. Kalacheva E. G., Voloshina E. V., Bogatko N. P. & Yaramchuk V. P. Hydrochemical regime of Nalychevo thermal springs (Kamchatka Peninsula). In *Volcanism and Related Processes. Proceedings of the XXIII Annual Scientific Conference dedicated to the Day of Volcanologist, Petropavlovsk-Kamchatsky, Russia*, 175–178 (2020).

Author contributions

I.K., developed methodology, produced most of the figures and wrote most of the text. O.B.-K. prepared the review and was responsible for interpretation. M.V. performed data processing and produced synthetic tests. A.J. determined the concept of the research and was responsible for data collection. All authors reviewed the manuscript and agreed with submission of this version.

Funding

This study was supported by the Russian Science Foundation Grant #20-17-00075P and the basic research project #FWZZ-2022-0017.

Declarations

Competing interests

The authors declare no competing interests.

Additional information

Correspondence and requests for materials should be addressed to I.K.

Reprints and permissions information is available at www.nature.com/reprints.

Publisher's note Springer Nature remains neutral with regard to jurisdictional claims in published maps and institutional affiliations.

Open Access This article is licensed under a Creative Commons Attribution-NonCommercial-NoDerivatives 4.0 International License, which permits any non-commercial use, sharing, distribution and reproduction in any medium or format, as long as you give appropriate credit to the original author(s) and the source, provide a link to the Creative Commons licence, and indicate if you modified the licensed material. You do not have permission under this licence to share adapted material derived from this article or parts of it. The images or other third party material in this article are included in the article's Creative Commons licence, unless indicated otherwise in a credit line to the material. If material is not included in the article's Creative Commons licence and your intended use is not permitted by statutory regulation or exceeds the permitted use, you will need to obtain permission directly from the copyright holder. To view a copy of this licence, visit <http://creativecommons.org/licenses/by-nc-nd/4.0/>.

© The Author(s) 2025